# Diagnostic based modeling for determining absolute atomic oxygen densities in atmospheric pressure helium-oxygen plasmas

Niemi, K., Reuter, S., Graham, L. M., Waskoenig, J., & Gans, T. (2009). Diagnostic based modeling for determining absolute atomic oxygen densities in atmospheric pressure helium-oxygen plasmas. Applied Physics Letters, 95(15), 151504-151504-3. [151504]. DOI: 10.1063/1.3242382

**Published in:**
Applied Physics Letters

# Diagnostic based modeling for determining absolute atomic oxygen densities in atmospheric pressure helium-oxygen plasmas

K. Niemi,[a] S. Reuter, L. M. Graham, J. Waskoenig, and T. Gans
*Centre of Plasma Physics, Queen's University Belfast, Belfast BT7 1NN, Northern Ireland, United Kingdom*

(Received 25 August 2009; accepted 14 September 2009; published online 15 October 2009)

Absolute atomic oxygen ground state densities in a radio-frequency driven atmospheric pressure plasma jet, operated in a helium-oxygen mixture, are determined using diagnostic based modeling. One-dimensional numerical simulations of the electron dynamics are combined with time integrated optical emission spectroscopy. The population dynamics of the upper O $3p\ ^3P$ ($\lambda=844$ nm) atomic oxygen state is governed by direct electron impact excitation, dissociative excitation, radiation losses, and collisional induced quenching. Absolute values for atomic oxygen densities are obtained through comparison with the upper Ar $2p_1$ ($\lambda=750.4$ nm) state. Results for spatial profiles and power variations are presented and show excellent quantitative agreement with independent two-photon laser-induced fluorescence measurements. © *2009 American Institute of Physics*.
[doi:10.1063/1.3242382]

The production of reactive atomic oxygen in cold atmospheric pressure plasmas promises high potential for technological exploitation and is targeted for many temperature sensitive surface treatments in biomedicine.[1,2] Reliable determination of absolute atomic oxygen densities is vital for plasma source development and understanding of fundamental mechanisms. Recently, atomic oxygen densities have been measured using two-photon absorption laser-induced fluorescence (TALIF) spectroscopy.[3–5] This technique is, however, highly intricate and experimentally limited to plasma source designs providing extensive diagnostic access. Simpler less demanding techniques such as model predictions or optical emission spectroscopy (OES) are highly requisite. Modeling plasma chemistry at atmospheric pressure is particularly ambiguous due to the multitude of possible reactions with vaguely known or even ill-defined reaction rates, in particular for three-body collisions and surface interactions. OES of cold atmospheric pressure plasmas is significantly hampered: high collision rates outbalance optical transition rates and the electron impact excitation processes are complex due to the pronounced and highly nonequilibrium electron dynamics.

The most versatile approach is diagnostic based modeling through active combination of numerical simulations and relatively simple time integrated OES. The electron dynamics is obtained using a one-dimensional numerical simulation based on fluid equations with a kinetic treatment of electrons. The resulting effective electron impact excitation rates are only insignificantly dependent on details of the plasma chemistry. Absolute atomic oxygen densities are subsequently determined using these effective excitation rates in combination with the optical emission from atomic oxygen and argon. In the following, details of this technique are discussed for a micro-scale radio-frequency (rf) driven atmospheric pressure plasma jet (APPJ) operated in a helium-oxygen mixture. The atomic oxygen densities are compared with results from independent TALIF measurements.[6]

The investigated $\mu$APPJ provides excellent optical access and is ideally suited for diagnostics development.[7] It produces a cold homogeneous $\alpha$-mode glow discharge at ambient pressure. The setup consists of two plane parallel stainless steel electrodes capped with quartz windows along the sides, forming a core plasma channel of 30 mm length and $1\times1$ mm$^2$ cross section. In this study, a fixed feed gas composition is used: 1 slm He with 0.5% $O_2$ and 0.1% Ar admixtures. The jet is driven at 13.56 MHz with up to 65 W rf generator power.

Optical emission spectra of the core plasma are recorded with a sensitivity calibrated spectrograph (430 to 950 nm, 0.5 nm resolution). The emission is collected perpendicular to the plasma channel with an effective spatial resolution of 1.4 mm. Consequently a time and space average across the discharge gap is obtained.

The time dependent intensity of the selected $\lambda=844$ nm atomic oxygen emission line resulting from direct electron-impact excitation is given by $I(t)=h\nu A_{ik}n_{exc}(t)$, where $h\nu$ denotes the photon energy, $A_{ik}$ the Einstein coefficient for spontaneous emission, and $n_{exc}$ the population density of the excited O($3p\ ^3P$) state. The dynamics within an rf cycle follows the differential equation $\dot{n}_{exc}(t)=k_e(t)n_e(t)n_{grd}-(A_i+Q_i)n_{exc}(t)$. Here, $n_e$ denotes the electron density, $n_{grd}$ the temporally constant ground state density, $A_i=\Sigma_j A_{ij}$ the optical decay rate of the upper state, and $Q_i$ the effective collisional quenching as described below. The excitation rate coefficient $k_e=\int f(\epsilon)\sigma(\epsilon)v_e d\epsilon$ depends on the normalized electron energy distribution function (EEDF) $f(\epsilon)$ and the electron impact excitation cross section $\sigma(\epsilon)$; $v_e=(2\varepsilon/m_e)^{0.5}$ denotes the electron velocity. It can be shown that the time averaged line intensity is finally given by $\langle I\rangle_t=h\nu a_{ik}\langle k_e n_e\rangle_t n_{grd}$, where $a_{ik}=A_{ik}/A_i$ denotes the optical branching ratio of the transition.

The observation volume and the solid angle can be accounted for by normalizing the measured optical emission from atomic oxygen to the $\lambda=750.4$ nm emission signal from a defined trace admixture of inert argon. This classical actinometry concept implies that the excited states, are not populated via cascades from higher levels, by excitation

[a]Electronic mail: k.niemi@qub.ac.uk.

 

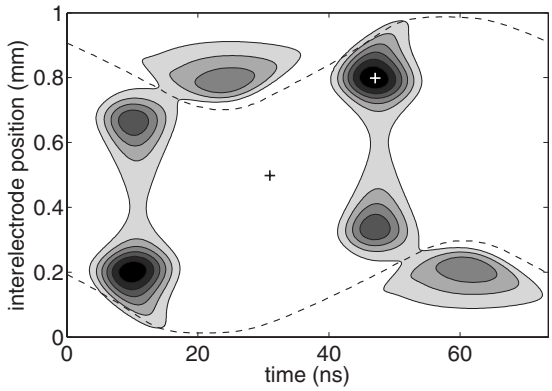


FIG. 1. Simulated time and space resolved Ar($2p_1$) electron-impact excitation rate on a linear gray scale starting from zero. The dashed curves indicate the sheath edges.

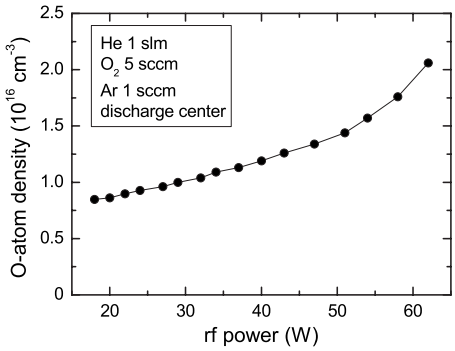


FIG. 3. O density in the discharge center as a function of rf generator power.

from lower metastable states, via dissociation, by collisional transfer, and reabsorption of radiation, and are not depopulated by collisional quenching.[8] Under the assumption that the electron-impact excitation cross sections have the same shape and threshold, the ratio of the excitation rates is independent of the plasma conditions. This approach can provide a qualitative measurement of the atomic oxygen ground state density in low pressure plasmas with not too low degree of dissociation.[9] The determination of absolute O-atom densities in cold atmospheric pressure plasmas is, however, significantly more complex.

Collisional-induced quenching of the upper O($3p\ ^3P$) and Ar($2p_1$) states outbalances optical transition rates and needs to be accounted for. The effective optical branching ratios of the corresponding transitions are calculated on the basis of quenching coefficients[3,10] for the feed gas composition according to $a_{ik}=A_{ik}/(A_i+\Sigma_q k_{iq} n_q)$, where $k_{iq}$ denotes the quenching rate coefficient for a collider density $n_q$.

The thresholds for direct electron-impact excitation of O($3p\ ^3P$) at 10.98 eV and of Ar($2p_1$) at 13.48 eV are similar. The difference of 2.5 eV is, however, critical for atmospheric pressure plasmas, where low mean electron energies and significant variations of the EEDF in the range of these thresholds are expected. The validity of classical actinometry—a constant ratio of the corresponding direct electron impact rates—is clearly not given in the present case. Classical actinometry also does not include the dissociative electron-impact excitation process, here $e+O_2 \rightarrow O(3p\ ^3P)+O+e$. The corresponding cross section has a higher threshold of 16.3 eV and a smaller maximum value at far higher electron energies compared to the direct channel. Nevertheless, dissociative excitation can become even dominant toward lower dissociation degrees.[9] The corresponding formal extension of the actinometry approach is possible. However, detailed information on the time and space dependent EEDF in the relevant energy range is required for quantitative density determination.

The electron energy distribution function is estimated using a one-dimensional numerical simulation based on fluid equations with a semikinetic treatment of electrons.[11] The input data of the model are kinetic reaction rates and transport coefficients calculated as a function of gas mixture and mean electron energy using the two-term approximation (TTA) Boltzmann solver Bolsig+.[12] The number of considered species (He, $He^*$, $He^+$, $He_2^*$, $He_2^+$, $O_2$, and $O_2^+$) and reactions (17 in total) are purposely kept minimum since details of the plasma chemistry and resulting atomic oxygen densities are represented in the measured optical emission signal. Since only the slope in the relevant energy range of the excitation thresholds is required, a rather simple numerical simulation of the electron properties without inclusion of chemical reactions is sufficient. For a given rf voltage amplitude the model yields the following electron properties as a function of time and space: electron density, mean electron energy, and the TTA EEDF that can be used to calculate electron-impact excitation rate.

Figure 1 shows the spatio-temporal characteristics of the excitation rate of the Ar($2p_1$) state along the electrode gap for one rf cycle with a voltage amplitude of 245 V. In each half cycle three excitation maxima are observed. The strongest can be attributed to the sheath collapse. The maximum occurring simultaneously indicate the sheath expansion at the opposite electrode. The maximum within the plasma boundary sheath is due to secondary electron multiplication by high electric fields in this region. The structures of these three excitation mechanisms correspond well to the results of independent simulations[13] and experimental observations.[14]

Since the OES measurements are time and space integrated across the electrode gap, yet the electron dynamics on the rf time scale and submillimeter space scale is strongly pronounced, the evaluation needs to be based on adequate effective excitation rates. Important for the present study is that the model reliably yields the time and space averaged EEDF $\langle n_e f(\epsilon)\rangle_{x,t}$ in the relevant range of the excitation thresholds. This holds independent of the extent to which chemical reactions are included in the model: they run on a slower time scale and the recoupling to the averaged EEDF is negligible. Figure 2 shows the resulting time and space averaged EEDF without consideration of chemical reactions. Also shown are, the temporal and local EEDF at minimal excitation in the bulk region and at maximal excitation in the sheath collapse region, as marked by crosses in Fig. 1. There is a pronounced group of low energy electrons trapped by the ambipolar potential during the whole rf cycle. Excitation and emission are dominantly caused by the midenergy electrons resulting from the sheath heating mechanisms. These features are consistent with particle-in-cell simulations.[15]

The effective excitation rate coefficients $k_e^*$, adequately describing the time and space integrated optical emission measurements, are calculated on the basis of the averaged EEDF using the cross section data from Refs. 16–18 according to $k_e^*=\langle n_e\rangle_{x,t}^{-1}\int\langle n_e f(\epsilon)\rangle_{x,t}\sigma(\epsilon)v_e d\epsilon$. Subsequently, the ratios $k_{Ar,e}^*/k_{O,e}^*=0.32$ and $k_{O,de}^*/k_{O,e}^*=9\times10^{-3}$ are derived. The in-

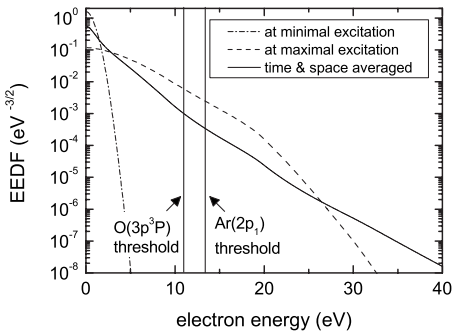


FIG. 2. Calculated electron energy distribution function. Time and space of minimal and maximal excitation is marked in Fig. 1 by crosses.

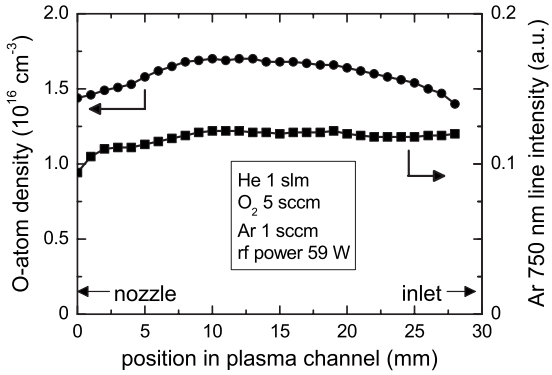


FIG. 4. O density and Ar 750 nm line intensity along the discharge channel.

dices *e* and *de* denote direct and dissociative excitation, respectively. The difference in the ratios of whether chemical reactions are included in the model or not is below 3%. The O-atom density is finally evaluated according to

$$n_O = \frac{I_O}{I_{Ar}} \frac{h\nu_{Ar}}{h\nu_O} \frac{k^*_{Ar,e}}{k^*_{O,e}} \frac{a_{Ar}}{a_O} n_{Ar} - \frac{k^*_{O,de}}{k^*_{O,e}} n_{O2}, \quad (1)$$

where *a* denotes the effective optical branching ratio. On the right hand side of Eq. (1), the first term is formally equal to the classical actinometry approach, while the second term represents the dissociative channel correction. The dependence of the ratio of the excitation rate coefficients on the rf power is considered. The dependencies of the rf power and maximum bulk electron density on the rf voltage amplitude exhibit a linear increase up to 225 V followed by an overlinear increase, see e.g., Fig. 2 of Ref. 13. This point is attributed to the onset of the $\gamma$ effect. The ratio of the direct excitation rates increases by less than 5% in the linear $\alpha$ regime. The corresponding increase in the dissociative ratio is about 25%. This is of minor relevance, since the dissociative correction of the atomic density stays below 8%.

Depletion of the ground state $O_2$ is not included in the model. The highest O-atom density observed, $2 \times 10^{16}$ cm$^{-3}$, corresponds to a maximal $O_2$ depletion of 10% at a gas temperature of 345 K (spectroscopically measured). Since the electron-impact excitation cross sections of $O_2$ and O in the range of 11 to 13.5 eV, are of similar value, about $1 \times 10^{-20}$ m$^2$, we assume that the lack of molecules is partially compensated by the dissociated atoms, thus, the resulting influence on the averaged EEDF as well as on the ratio of the effective rate coefficients to be marginal.

The O-atom density measured in the center of the discharge channel as a function of the rf generator power is shown in Fig. 3. The plasma ignites at 25 W power and spreads over the entire electrode length. Once ignited, the plasma can be sustained down to 18 W. The O-atom density increases linearly with power from $0.8 \times 10^{16}$ to $1.4 \times 10^{16}$ cm$^{-3}$ at 50 W. At higher powers, the plasma no longer operates in a pure $\alpha$ mode, and an overlinear increase is observed. At a power of about 65 W, the plasma switches to a spatially constricted mode with a high current density. Consistent results were found by independent TALIF measurements on a similar setup:[6] an initial O-atom density of $0.7 \times 10^{16}$ cm$^{-3}$ and a similar power dependence. The operational power range differs due to the rf equipment used.

Figure 4 shows the atomic oxygen density along the plasma channel. The nozzle defines the zero position and the gas inlet is at 30 mm. The atomic oxygen density increases from $1.4 \times 10^{16}$ cm$^{-3}$ to approach a constant value of $1.7 \times 10^{16}$ cm$^{-3}$ after a distance of 10 mm. In contrast, the 750 nm argon line intensity probing the electron properties already reaches a constant value within the first 2 mm, see Fig. 4. The atomic oxygen production and destruction equilibrium can therefore be attributed to the slower chemical rection processes. The corresponding build-up time is ≈0.6 ms accordingly to the gas velocity of ≈17 ms$^{-1}$. At 10 mm distance to the nozzle the O-atom density as well as the argon emission starts decreasing. This effect is most likely caused by ambient air species backdiffusing from the nozzle into the plasma. The same trends were found by independent TALIF measurements[6] as well as a coinciding value for the absolute O-atom density.

The authors acknowledge support by a Science and Innovation award of the EPSRC. One author (L.M.G) is supported by DEL. We thank Nikolas Knake and Volker Schulz-von der Gathen (Ruhr-Universität Bochum) for valuable discussion.

[1] E. Stoffels, I. E. Kieft, R. E. J. Sladek, L. J. M. van den Bedem, E. P. van der Laan, and M. Steinbuch, Plasma Sources Sci. Technol. **15**, S169 (2006).
[2] R. Foest, E. Kindel, H. Lange, A. Ohl, M. Stieber, and K.-D. Weltmann, Contrib. Plasma Phys. **47**, 119 (2007).
[3] K. Niemi, V. Schulz-von der Gathen, and H. F. Döbele, Plasma Sources Sci. Technol. **14**, 375 (2005).
[4] S. Reuter, K. Niemi, V. Schulz-von der Gathen, and H. F. Döbele, Plasma Sources Sci. Technol. **18**, 015006 (2009).
[5] N. Knake, St. Reuter, K. Niemi, V. Schulz-von der Gathen, and J. Winter, J. Phys. D: Appl. Phys. **41**, 194006 (2008).
[6] N. Knake, K. Niemi, S. Reuter, V. Schulz-von der Gathen, and J. Winter, Appl. Phys. Lett. **93**, 131503 (2008).
[7] V. Schulz-von der Gathen, V. Buck, T. Gans, N. Knake, K. Niemi, St. Reuter, L. Schaper, and J. Winter, Contrib. Plasma Phys. **47**, 510 (2007).
[8] J. W. Coburn and M. Chen, J. Appl. Phys. **51**, 3134 (1980).
[9] R. E. Walkup, K. L. Saenger, and G. S. Selwyn, J. Chem. Phys. **84**, 2668 (1986).
[10] N. Sadeghi, D. W. Setser, A. Francis, U. Czarnetzki, and H. F. Döbele, J. Chem. Phys. **115**, 3144 (2001).
[11] Y. Sakiyama and D. B. Graves, J. Phys. D: Appl. Phys. **39**, 3644 (2006).
[12] G. J. M. Hagelaar and L. C. Pitchford, Plasma Sources Sci. Technol. **14**, 722 (2005).
[13] J. J. Shi and M. G. Kong, J. Appl. Phys. **97**, 023306 (2005).
[14] V. Schulz-von der Gathen, L. Schaper, N. Knake, S. Reuter, K. Niemi, T. Gans, and J. Winter, J. Phys. D: Appl. Phys. **41**, 194004 (2008).
[15] F. Iza, J. K. Lee, and M. G. Kong, Phys. Rev. Lett. **99**, 075004 (2007).
[16] J. E. Chilton, J. B. Boffard, R. S. Schappe, and C. C. Lin, Phys. Rev. A **57**, 267 (1998).
[17] M. B. Schulman, F. A. Scharpton, S. Chung, C. C. Lin, and L. W. Anderson, Phys. Rev. A **32**, 2100 (1985).
[18] R. R. Laher and F. R. Gilmore, J. Phys. Chem. Ref. Data **19**, 277 (1990).